Mixing Driven by Critical Reflection of Near-Inertial Waves over the Texas–Louisiana Shelf

LIXIN QU,[a,b] LEIF N. THOMAS,[a] ROBERT D. HETLAND,[b] AND DAIJIRO KOBASHI[c]

[a] *Department of Earth System Science, Stanford University, Stanford, California*
[b] *Pacific Northwest National Laboratory, Richland, Washington*
[c] *Department of Oceanography, Texas A&M University, College Station, Texas*

(Manuscript received 5 January 2022, in final form 6 July 2022)

ABSTRACT: Studies of internal wave-driven mixing in the coastal ocean have been focused on internal tides, while wind-driven near-inertial waves (NIWs) have received less attention in this regard. This study demonstrates a scenario of NIW-driven mixing over the Texas–Louisiana shelf. Supported by a high-resolution simulation over the shelf, the NIWs driven by land–sea breeze radiate downward at a sharp front and enhance the mixing in the bottom boundary layer where the NIWs are focused because of slantwise critical reflection. The criterion for slantwise critical reflection of NIWs is $\omega = \sqrt{f^2 + s_{\text{bot}}^2 N^2 (1 - s_\rho / s_{\text{bot}})}$ (where ω is the wave frequency, s_{bot} is the bottom slope, and s_ρ is the isopycnal slope), under the assumption that the mean flow is in a thermal wind balance and only varies in the slope-normal direction. The mechanism driving the enhanced mixing is explored in an idealized simulation. During slantwise critical reflection, NIWs are amplified with enhanced shear and periodically destratify a bottom boundary layer via differential buoyancy advection, leading to periodically enhanced mixing. Turbulent transport of tracers is also enhanced during slantwise critical reflection of NIWs, which has implications for bottom hypoxia over the Texas–Louisiana shelf.

KEYWORDS: Coastal flows; Inertia–gravity waves; Mixing

1. Introduction

The classic view of mixing in the coastal ocean comprises a surface boundary layer, primarily mixed through wind stress and surface gravity wave breaking, and a bottom boundary layer, primarily mixed through either tides or near-bottom mean flows. Of 3.5 TW of tidal energy, 2.6 TW is dissipated in shallow seas and shelves (Wunsch and Ferrari 2004), suggesting that barotropic tides are an important source of bottom mixing in the coastal ocean. Internal tides are another source of bottom mixing, but this is thought to be isolated to specific geometries and wave conditions (Kunze and Smith 2004; MacKinnon et al. 2017). Moreover, the processes controlling the bottom boundary layer through either wind stress or subinertial flow are indirect and confounded by other shelf processes. Wind-driven currents are thought be confined to the surface boundary layer, with the primary mechanisms for driving flow in the geostrophic interior being convergence and associated sea level setup (divergence causing setdown), which is then communicated over depth through a barotropic pressure gradient. This may excite continental shelf waves (e.g., the review by Brink 1991), which can be bottom intensified and modulate bottom mixing. Unforced baroclinic flows may be altered by buoyancy arrest (MacCready and Rhines 1991; Chapman and Lentz 1994; Yankovsky and Chapman 1997), which will reduce the magnitude of the near bottom currents, reducing the bottom stress and thickness of the bottom boundary layer.

As an intermediary driven by winds, near-inertial waves (NIWs) can communicate surface wind-driven energy to bottom boundary layers, enhance bottom mixing, and alter the properties of bottom waters. Vertical propagation of NIWs in the coastal ocean has been observed in many regions, such as New Jersey inner shelf (Chant 2001), California coast (Lerczak et al. 2001), New England shelf (MacKinnon and Gregg 2005), and Tasmanian shelf (Schlosser et al. 2019). A modeling study of the NIWs on the Oregon continental shelf (Federiuk and Allen 1996) finds that the near-inertial energy is concentrated over the bottom under upwelling conditions when the NIWs undergo critical reflection, potentially leading to enhanced bottom mixing.

On the Texas–Louisiana shelf in the northern Gulf of Mexico, notable land–sea breeze during summer resonantly forces near-inertial motions over the shelf and inputs a large amount of energy into the NIW field (DiMarco et al. 2000). The input of freshwater from the Mississippi–Atchafalaya river system generates a baroclinic current over the shelf out to approximately 50-m depth (Zhang et al. 2012; Z. Zhang et al. 2014) that contains a rich eddy field due to baroclinic instabilities within the river plume (Hetland 2017). The fronts in the eddy field provide the pathways through which the NIWs communicate surface wind-driven energy to the bottom boundary layer (Qu et al. 2021b). Moreover, front passage is rare during summer in this region, winds during nonstorm periods are weak, and thereby surface gravity waves do not strongly impact the bottom boundary layer deeper outside of the nearshore region (Xu et al. 2011). Tides are also relatively weak over the shelf. Consequently, the Texas–Louisiana shelf is an ideal geophysical laboratory to isolate the process of NIW-induced bottom mixing.

This study explores the critical reflection of NIWs over the Texas–Louisiana shelf and demonstrates the mechanism

Corresponding author: Lixin Qu, lixinqu123@gmail.com

DOI: 10.1175/JPO-D-22-0004.1

driving enhanced bottom mixing upon the critical reflection. As a counterpart to the well-studied case of the critical reflection of internal tides (Cacchione et al. 2002; Nash et al. 2004; Kunze and Smith 2004), this study complements the scenario of internal-wave-driven mixing in the coastal ocean. The paper is organized as follows. In section 2 we introduce the realistic simulation on the Texas–Louisiana shelf illustrating the critical reflection of NIWs and the enhanced mixing. In section 3 we derive and discuss the criterion for slantwise critical reflection of NIWs. In section 4 we show how the slantwise critical reflection near-inertially enhances bottom mixing based on the idealized simulations. In section 5 we discuss how the slantwise critical reflection modifies bottom environments such as bottom hypoxia.

2. Realistic simulation

The Mississippi River and Atchafalaya River create a large plume of buoyant freshwater on the Texas–Louisiana shelf. In addition, a notable land–sea breeze persists over the shelf during summertime, which is diurnal and hence nearly resonant with the local inertial period (the local inertial period is about 24 h near 30°N). As a consequence, strong near-inertial oscillations are resonantly energized in the surface mixed layer, with observed amplitudes reaching 0.5 m s^{-1} (DiMarco et al. 2000). Under the interaction with the river plume, the surface near-inertial energy can be radiated downward via NIWs, potentially enhancing bottom mixing and alter bottom properties (Qu et al. 2021b). A high-resolution simulation in the Texas–Louisiana shelf is conducted to investigate the propagation of NIWs and the associated bottom mixing. In this section we describe the model configuration and the findings revealed in the simulation.

a. *Model configuration*

A nested model was developed for the Texas–Louisiana shelf (Fig. 1a). The model domain was selected for the region of active submesoscale currents (Kobashi and Hetland 2020). The nested model exchanges variables along the boundaries between the parent and child models, and thus, the exchange between grids is two-way.

The parent domain covers the entire Texas–Louisiana shelf and its slopes (Fig. 1a). The model uses a curvilinear grid stretching along the coastline of Texas and Louisiana horizontally and terrain-following stretching coordinate (s coordinate) vertically. The finest horizontal resolution is approximately 650 m, and the coarsest resolution is approximately 3.7 km. The number of vertical layers N is 30, and more layers are concentrated near the surface and bottom to ensure the adequate number of layers in the surface and bottom boundary layers. As with the previous incarnations of this model configuration (Hetland and DiMarco 2012; Zhang et al. 2012), tides are not included because they are very weak over the TXLA shelf (DiMarco and Reid 1998). The shelf model is nested into Global HYCOM Reanalysis, which has a spatial resolution of approximately 9 km. Surface forcing and fluxes are obtained from ERA-Interim (Dee et al. 2011). A total of nine rivers, namely, Sabine, San Antonio, Trinity, Brazos, Calcasieu, Lavaca, and Nueces as well as the Mississippi and Atchafalaya, two major rivers connected to the shelf, are included. The streamflow data were obtained from U.S. Army Corps of Engineers and U.S. Geological Survey. Salinity of the rivers is set to zero, and streamflow temperature is estimated from air temperature using a bulk formula based on Stefan and Preud'homme (1993). The model uses third-order upwind scheme (horizontal) and fourth-order centered scheme (vertical) for momentum advection and MPDATA (Multidimensional Positive Definite Advection Transport Algorithm) for tracer advection (Smolarkiewicz 2006). The vertical mixing scheme used is k–ω, a generic length scale (GLS) turbulent closure model (Umlauf and Burchard 2003). The k–ω and other GLS schemes (e.g., k–ϵ) have been widely used in coastal ocean modeling including simulating estuaries (Warner et al. 2005a; Ralston et al. 2010), river plumes (Zhang et al. 2004; Hetland 2005), and shelf dynamics (Jacox and Edwards 2011; W. G. Zhang et al. 2014). Different GLS schemes exhibit similar performance in parameterizing vertical mixing (Warner et al. 2005b; Wijesekera et al. 2003) and demonstrate reasonable agreement with turbulent kinetic energy budgets from LES (Umlauf and Burchard 2003). A Laplacian diffusivity for horizontal mixing is applied with constant values of 5.0 m^2 s^{-1} for momentum and 1.0 m^2 s^{-1} for tracers, both of which were scaled with grid size.

The child domain was created from the parent domain, and therefore the bathymetry and s-grid parameters of the child grid including the number of vertical sigma layers ($N = 30$) is the same as the parent's. The bathymetry of the child domain was obtained by linearly interpolating the bathymetry of the parent domain. The ratio of the nesting is 5 to 1, and the grid resolution of the child grid is roughly 300 m. The surface fluxes, open boundaries, and initial conditions were also obtained from the parent model by interpolating the parent model's outputs to the child grid. By doing so, the model can reduce initial shocks typically seen at the beginning of the simulation. The parent and child models were run for the period from 1 June to 26 July 2010 (roughly 6 weeks). Both models provide sea surface height, current velocity, temperature, salinity, dissolved oxygen (DO), and mixing parameters including momentum and salt diffusivity, TKE, and general length scale. DO was treated as a tracer: Bottom oxygen fluxes were estimated based on an oxygen respiration model developed by Hetland and DiMarco (2008), and the surface DO fluxes were estimated based on Weiss (1970) by assuming that surface DO is always saturated. DO was also included for point sources (i.e., rivers) in the same way as the surface boundary conditions. Despite the simplification, the model is able to replicate temporal and spatial variability of DO on the shelf (Fennel et al. 2016). The output frequency is 1 h.

b. *Critical reflection of NIWs off the Texas–Louisiana shelf*

The Mississippi–Atchafalaya plume is unstable to baroclinic instabilities, generating a rich field of eddies over the continental shelf. Figure 1 shows a typical scenario of the eddies on the shelf in summer based on the realistic simulation. The eddies are quintessentially anticyclones surrounded by filaments of cyclonic

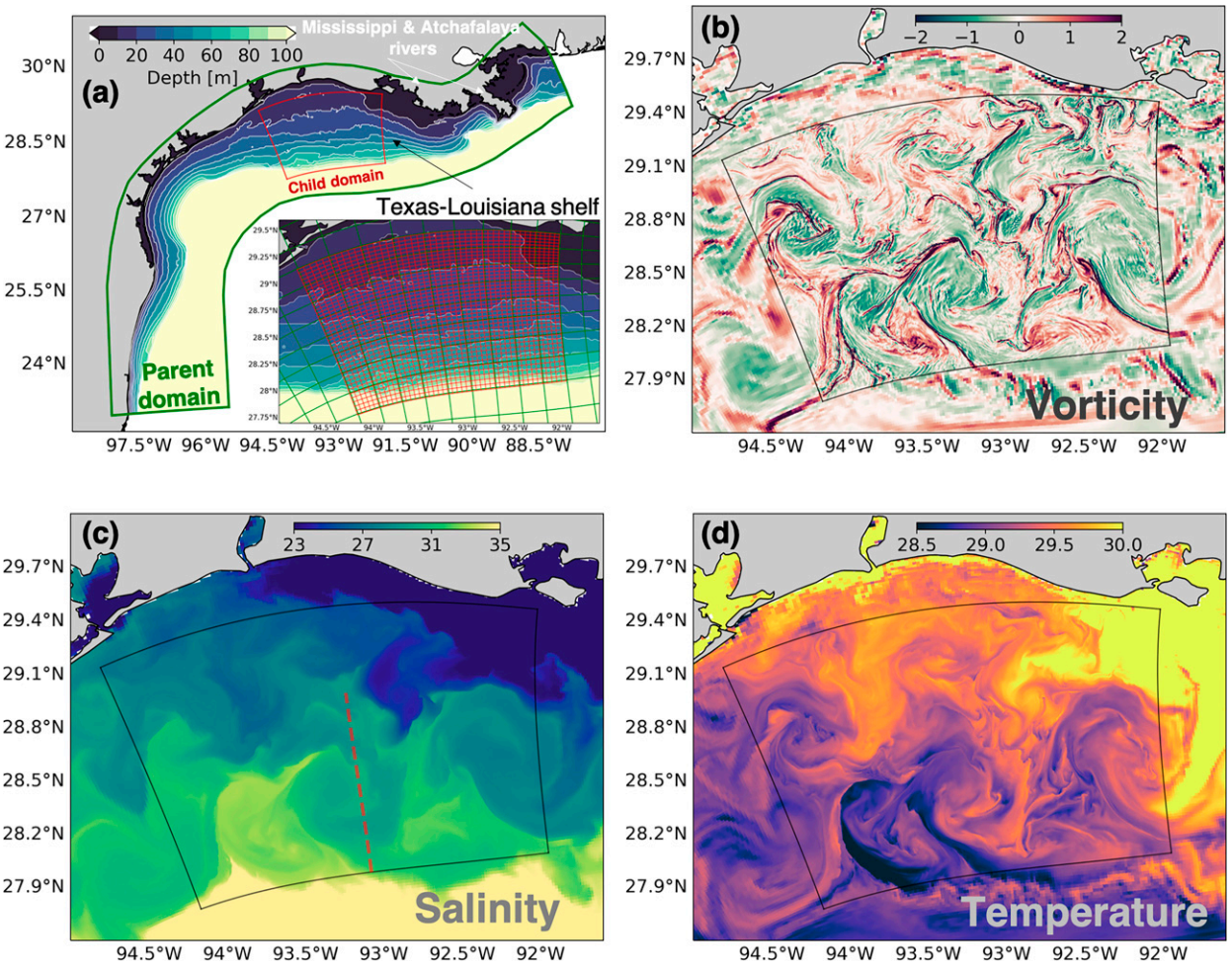

FIG. 1. (a) TXLA parent and child model domains. The inset at the lower-right corner is the zoomed-in view of the child domain. The child and parent grids are shown in red and green, respectively, with every 15th grid point shown. Also shown are snapshots of (b) surface relative vorticity ζ/f, (c) salinity, and (d) temperature made at 1700 UTC 8 Jun 2010. The gray-outlined box marks the boundaries of the child domain. The child model output is shown within the box, and the parent model output is shown outside of it. The section selected for later analysis is denoted by the red dashed line in (c).

vorticity, indicating sharp gradients of vorticity at the peripheries (Fig. 1b). They are characterized by freshwater in the cores, and the density field is salinity controlled (instead of temperature controlled), because the variation in temperature is small (Figs. 1c,d).

In addition, the land–sea breeze energizes strong near-inertial oscillations in the surface mixed layer. However, the energy of the near-inertial motions is not retained within the surface mixed layer. Instead, the energy radiates downward in the form of NIWs through interactions with the eddies. The process is referred to as ζ refraction, through which the horizontal wavelength of the NIWs is reduced due to the sharp vorticity gradients around the eddies and hence their downward radiation is facilitated (Young and Jelloul 1997; van Meurs 1998; Lee and Niiler 1998; Asselin and Young 2020; Thomas et al. 2020). A typical scenario of the downward radiation of NIWs is shown in Fig. 2. When looking into a 1-week period from 3 to 10 June, we can see that the winds exhibit a diurnal (near inertial) signal in the first 2 or 3 days (Fig. 2a). Correspondingly, the currents at the surface resonantly derive their energy from the winds, resulting in significant near-inertial oscillations (Fig. 2b). Subsequently, the near-inertial oscillations are transformed into vertically propagating NIWs. The NIWs radiate from the surface, propagate downward, and approach the bottom, the pathway of which is demonstrated by the tilted shear bands (Figs. 2e,f).

As the NIWs approach the bottom, the NIWs can get reflected with an altered pathway. Ray tracing is conducted to illustrate the process of the wave reflection off the bottom (Fig. 3). The ray-tracing method follows Whitt and Thomas (2013) and yields wave characteristics based on the dispersion relation of NIWs in baroclinic currents. The ray-tracing solution replicates the wave pathway that is indicated by the titled shear bands shown in Figs. 2e and 2f. More important, the solution suggests that the waves undergo critical reflection near the bottom, upon which the wave rays are aligned

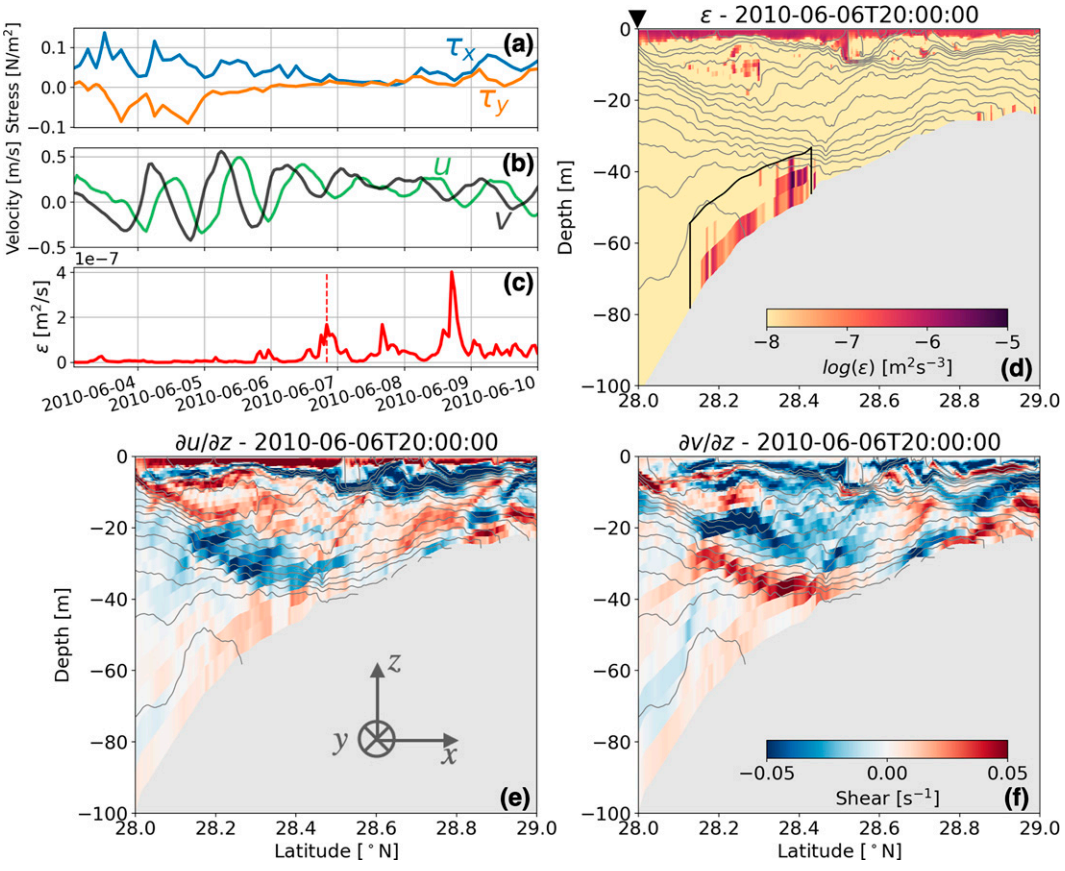

FIG. 2. Time series of (a) surface winds, (b) surface currents, and (c) TKE dissipation rate ϵ. The winds and currents are sampled at the southern end of the section [marked by the triangle in (d)], and ϵ is spatially averaged over a control volume above the bottom [marked by the outlined box in (d)]. Also shown are (d) ϵ and (e),(f) vertical shear along the section marked in Fig. 1c (u is the across-shelf velocity, and v is the along-shelf velocity). Isopycnals are contoured in gray every 0.5 kg m^{-3}. The snapshots are made at 2000 UTC 6 Jun 2010, which is marked in (c) by the vertical red dashed line.

with the shelf and compressed, and hence the wave energy is focused, potentially leading to turbulence and mixing. Consistently, the TKE dissipation rate ϵ is significantly elevated at the region where the wave rays are focused, indicating enhanced mixing (Fig. 2d). Moreover, the time series of the average ϵ (averaged at the region associated with the critical reflection) exhibits near-inertial responses of enhancement (Fig. 2c), indicating a strong link between the elevated mixing and the NIWs. Note that a slantwise critical layer with isopycnals running parallel to bathymetry exists in this section between 28.5° and 28.8°N, which is a trapping zone for NIWs (Qu et al. 2021b), but mixing is not enhanced there. The potential reason for the weak mixing is that the NIWs do not supply energy to the slantwise critical layer but reflect offshore and undergo near-critical reflection, which is suggested by the ray-tracing result.

3. Theory

In this section, we used a simplified theoretical model to derive the criterion for slantwise critical reflection of NIWs. The model consists of three elements: 1) a bottom-attached front, 2) a shelf, and 3) downward-propagating NIWs. A schematic of the model is shown in Fig. 4, and the elements are elaborated below.

For the bottom-attached front, we assume that it has a constant vertical buoyancy gradient $N^2 \equiv \partial \bar{b}/\partial z$, a constant horizontal buoyancy gradient $M^2 \equiv \partial \bar{b}/\partial x$ in the across-shore direction, where $b = -g(\rho/\rho_0)$ is the buoyancy (g is the acceleration due to gravity, ρ is the potential density, and ρ_0 is the reference density), and no gradient in the along-shore direction. We also assume that the background flow $\bar{v}$ is in thermal wind balance. This configuration induces a nonzero vertical shear $\partial \bar{v}/\partial z$ and hence a finite Richardson number Ri_g:

$$\frac{\partial \bar{v}}{\partial z} = M^2 f^{-1} \quad \text{and}$$

$$\mathrm{Ri}_g = N^2 \Big/ \left(\frac{\partial \bar{v}}{\partial z}\right)^2 = N^2 f^2 M^{-4}, \tag{1}$$

where f is the Coriolis parameter.

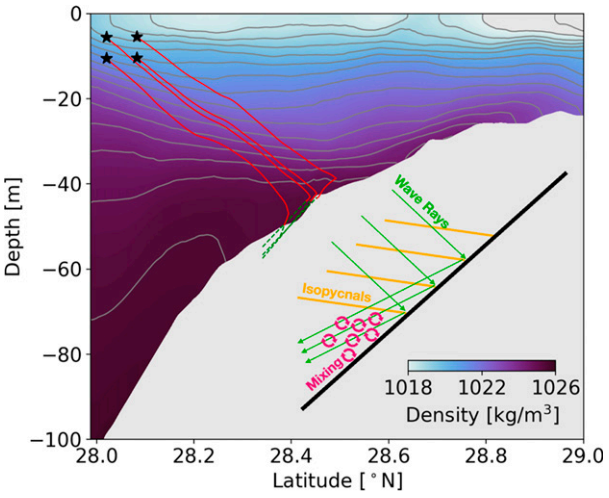

FIG. 3. Rays of NIWs. The black stars denote the initial locations of the waves. The red lines denote the wave characteristics/rays. The green dashed lines denote the extensions of the rays, indicating the heading of the waves. The ray-tracing calculation is based on the f-plane approximation with $f|_{\mathrm{Lat}=28.5°\mathrm{N}}$. The background density field used in the ray-tracing calculation is the potential density along the section marked in Fig. 1c, which is averaged from 5 to 10 Jun 2010. The background flow is assumed to be in thermal wind balance. The wave frequency is set to $1.07f$. The mean potential density is shaded. Isopycnals are contoured in gray every 0.5 kg m^{-3}. A schematic illustrating near-critical reflection of NIWs is shown at the lower-right corner.

For the shelf, we assume that it is a linear slope with a constant tilting angle θ ($\theta > 0$ can be ensured by altering the orientation of the coordinates), and the depth only varies in the across-shore direction. We assume that $\bar{v}$ only varies in the direction normal to the bottom, and as a consequence of the sloping bathymetry, the balanced flow $\bar{v}$ is sheared in the across-shore direction, and this lateral shear depends on the bottom slope $s_{\mathrm{bot}} \equiv \tan\theta$ and M^2 (see the appendix for the details). This leads to a nonzero relative vorticity ζ and hence a nonzero Rossby number Ro_g:

$$\zeta = \frac{\partial \bar{v}}{\partial x} = -M^2 f^{-1} s_{\mathrm{bot}} \quad \text{and}$$

$$\mathrm{Ro}_g = \zeta/f = -M^2 f^{-2} s_{\mathrm{bot}}. \tag{2}$$

The baroclinicity (represented by Ri_g) and the relative vorticity (represented by Ro_g) of the front can modify the properties of NIWs and particularly alter the propagation pathways of the waves (Mooers 1975; Kunze 1985; Whitt and Thomas 2013). Under the modification, the slopes of the wave characteristics follow

$$\lambda_{\pm} = s_\rho \pm \sqrt{\frac{\omega^2 - \omega_{\mathrm{min}}^2}{N^2}}, \tag{3}$$

where $s_\rho \equiv -M^2/N^2$ is the isopycnal slope, ω is the wave frequency, and ω_{min} is the minimum frequency allowable for the waves. Following Whitt and Thomas (2013) with Eqs. (1) and (2), ω_{min} can be expressed as

$$\omega_{\mathrm{min}} = f\sqrt{1 + \mathrm{Ro}_g - \mathrm{Ri}_g^{-1}} = \sqrt{f^2 - s_{\mathrm{bot}} M^2 - M^4 N^{-2}}$$
$$= f\sqrt{1 - \mathrm{Sr}}, \tag{4}$$

where $\mathrm{Sr} \equiv M^2 f^{-2}(s_{\mathrm{bot}} - s_\rho)$ is the slope-relative Burger number (Qu and Hetland 2020). Note that $\mathrm{Sr} > 1$ is corresponding to negative Ertel potential vorticity (PV) where $\mathrm{PV}/(fN^2) = 1 - \mathrm{Sr}$ and hence represents the regime of symmetric or centrifugal instability (Thomas et al. 2013). In this study, we will only consider the stable regime with $\mathrm{Sr} < 1$. Critical reflection occurs when the rays of the reflected waves run parallel to the sloping

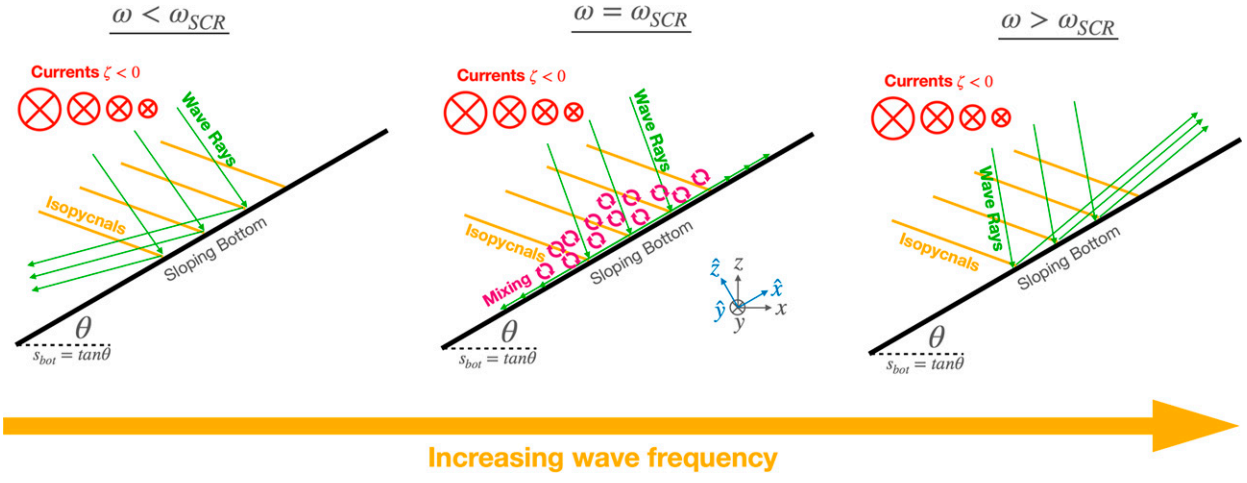

FIG. 4. Schematics illustrating (left) backward reflection, (center) critical reflection, and (right) forward reflection of NIWs in a buoyant front over a continental shelf. In the nonrotated coordinates, x is the horizontal, across-shore direction; y is the horizontal, alongshore direction; and z is the vertical direction. In the rotated coordinates, $\hat{x}$ is the across-slope direction and $\hat{z}$ is the slope-normal direction; $s_{\mathrm{bot}} = \tan\theta$ is the bottom slope.

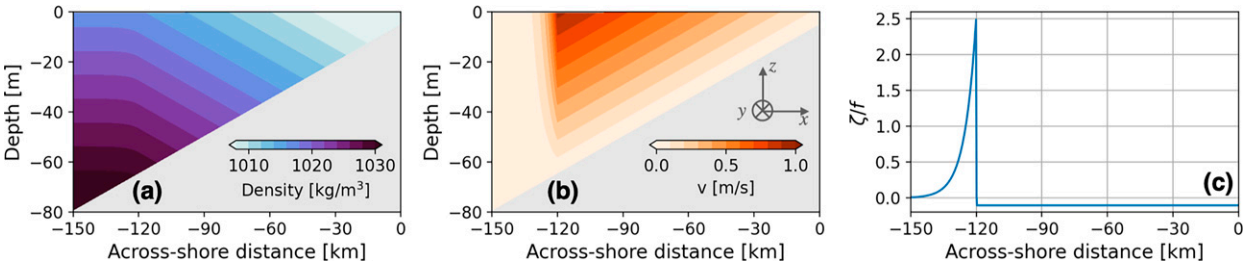

FIG. 5. Idealized model configuration: (a) initial density condition, (b) initial condition of alongshore velocity, and (c) initial surface relative vorticity.

bottom, that is, when either of $\lambda_{\pm}$ is equal to s_{bot}. This yields a frequency criterion for the slantwise critical reflection:

$$\omega_{\text{SCR}} = \sqrt{f^2 + s_{\text{bot}}^2 N^2 (1 - s_\rho / s_{\text{bot}})}. \tag{5}$$

This result depends on the assumption that the geostrophic flow only varies in the slope-normal direction. A more generic criterion without this assumption can be obtained by substituting s_{bot} in Eq. (30) of Whitt and Thomas (2013) as

$$\omega^*_{\text{SCR}} = \sqrt{f^2 (1 + \text{Ro}_g) + s_{\text{bot}}^2 N^2 (1 - 2 s_\rho / s_{\text{bot}})}, \tag{6}$$

which can reduce to Eq. (5) by substituting Ro_g with Eq. (2). Equation (5) reveals how the sloping bathymetry (s_{bot}), the bottom-attached front (through s_ρ and N^2), and the background rotation (f) set the frequency of the NIWs that undergo slantwise critical reflection. On the basis of this criterion, NIWs would undergo backward or forward reflection if the wave frequency is respectively less than or greater than ω_{SCR}, as illustrated in Fig. 4.

According to Eq. (5), the critical NIWs are superinertial in the scenarios of buoyant fronts (because $s_\rho < 0$ and $\omega_{\text{SCR}} > f$). Schematics of buoyant fronts are illustrated in Fig. 4, where light water is at shallower depths and dense water is at deeper depths (i.e., $M^2 > 0$ and $s_\rho < 0$). However, $\omega_{\text{SCR}} > f$ does not always hold true in the scenarios with dense fronts where the sloping bathymetry is retrograde with dense water at shallower depths and light water at deeper depths (i.e., $M^2 < 0$ and $s_\rho > 0$). One example of dense fronts is the dense shelf overflows (Yankovsky and Legg 2019). The parameter that controls whether NIWs undergo slantwise critical reflections that are superinertial ($\omega_{\text{SCR}} > f$) or subinertial ($\omega_{\text{SCR}} < f$) is the ratio between the isopycnal slope and the bottom slope s_ρ / s_{bot}; $\omega_{\text{SCR}} < f$ holds true if $s_\rho / s_{\text{bot}} > 1$, and vice versa. The critical NIWs can be inertial ($\omega_{\text{SCR}} = f$) when the topography is flat ($s_{\text{bot}} = 0$) and/or the isopycnals run parallel with the bathymetry ($s_\rho / s_{\text{bot}} = 1$), which have been investigated by Grisouard and Thomas (2015) and Qu et al. (2021b), respectively.

4. Idealized simulations

a. Idealized model configuration

An idealized model is built to test the criterion for the slantwise critical reflection and explore the mechanism driving the near-inertially enhanced mixing revealed by the realistic simulation. The model configuration is shown in Fig. 5. The idealized domain represents a continental shelf. The shelf has a constant slope of $s_{\text{bot}} = 5 \times 10^{-4}$, a value that is based on the characteristics of the Texas–Louisiana shelf. The depth increases linearly from 5 to 118 m in an across-shore distance of 226 km. The span of the shelf in the alongshore direction is set to be narrow (about 4 km) so that when combined with periodic boundary conditions all the properties tend to stay invariant in the alongshore direction.

The front in the idealized model is designed based on the characteristics of the front shown in Fig. 2. The across-shore buoyancy gradient of the front is set to a constant value, $M^2 = 10^{-6}\ \text{s}^{-2}$, in the region that is within 120 km of the shore. The magnitude of M^2 is set based on the statistics of the fronts over the Texas–Louisiana shelf during the summertime by Hetland (2017). The initial flow is in geostrophic balance. Because of the sloping bathymetry, the flow at $x \geq -120$ km is horizontally sheared with anticyclonic vorticity, as derived in section 3. In addition, M^2 exponentially decreases as one goes farther offshore (at $x < -120$ km), with an e-folding scale of 5 km. This leads to a sharp decay of the flow speed moving offshore, yielding a maximum of the vorticity gradient at $x = -120$ km (Fig. 5c) and hence creating a preferential location for NIWs to radiate downward. The stratification is set to a constant value $N^2 = 2 \times 10^{-3}\ \text{s}^{-2}$ for $z \geq -65$ m and exponentially decreases for $z < -65$ m, with an e-folding scale of 5 m. Setting N^2 and M^2 to be constant at $x \geq -120$ km is to emphasize and isolate the physics of slantwise critical reflection, the caveat of which leads to a larger range of density than the one in the realistic simulation. The configuration of the bathymetry and the front yields a minimum frequency allowable for NIWs as $0.89f$ at $x > -120$ km.

The idealized model is configured in ROMS (Shchepetkin and McWilliams 2005). The horizontal grid is 1026×18 with a resolution of 220 m $\times$ 220 m. The vertical grid has 64 terrain-following layers, with the stretching parameters being $\theta_S = 0.4$ and $\theta_B = 0.4$. Periodic conditions are applied at the alongshore open boundaries, and a sponge layer is set at the offshore open boundary to damp waves. The "MPDATA" scheme is used for the tracer advection (Smolarkiewicz 2006). The k–ϵ turbulence closure scheme is used to parameterize vertical mixing, and the Canuto A stability function formulation is applied (Umlauf and Burchard 2003; Canuto et al.

TABLE 1. Wind forcing configuration of the idealized ensemble runs.

f	Wind frequency/f	Wind stress amplitude
$f\|_{\text{Lat}=28.5°\text{N}}$	0.90, 0.95, 0.96, 0.98, 1.00, 1.02, 1.04, 1.05, 1.06, 1.08, 1.10, 1.12, 1.14, 1.15, 1.16, 1.18, 1.20, 1.22, 1.24, 1.25, and 1.30	4×10^{-2} N m^{-2}
—	0.90, 1.00, 1.10, 1.20, and 1.30	4×10^{-3} N m^{-2}

2001). The Coriolis parameter is set to $f|_{\text{Lat}=28.5°\text{N}}$ on the basis of the section shown in Fig. 2.

b. *Backward, critical, and forward reflection*

Given the bathymetry ($s_{\text{bot}} = 5 \times 10^{-4}$), the buoyancy gradients of the front ($N^2 = 2 \times 10^{-3}$ s^{-2} and $M^2 = 10^{-6}$ s^{-2}), and the rotation ($f|_{\text{Lat}=28.5°\text{N}}$), the critical frequency from Eq. (5) is calculated to be $\omega_{\text{SCR}} = 1.1f$. To test whether there is a critical reflection when the frequency of the winds is near ω_{SCR}, a group of experiments is conducted by forcing the idealized model with different winds. Oriented in the across-shore direction, all the winds are near-inertially oscillatory (sinusoidal) so that they can energize NIWs. To excite a range of NIWs, we set the winds to have different frequencies and amplitudes. The frequencies span from $0.9f$ to $1.3f$, covering the scenarios of backward reflection ($\omega < \omega_{\text{SCR}}$), critical reflection ($\omega = \omega_{\text{SCR}}$), and forward reflection ($\omega > \omega_{\text{SCR}}$). Two amplitudes, 4×10^{-2} N m^{-2} and 4×10^{-3} N m^{-2}, are used. Details of the wind forcing configuration are shown in Table 1.

Snapshots of the vertical shear and the ray-tracing solutions from a subset of the experiments are shown in Fig. 6. Consistent with the theory of ζ refraction, all experiments show downward radiation of NIWs near $x = -120$ km based on the patterns of the vertical shear. In addition, the wave pathways (indicated by the vertical shear) of the downward radiation and the reflection off the shelf generally agree with the ray-tracing solutions, which implies that the simulations reproduce the scenarios of the backward reflection, critical reflection, and forward reflection that the theory predicts.

To examine the dependence of bottom mixing on reflection scenarios, we compare the mean TKE dissipation rate from the experiments that are with the wave frequencies ranging from $0.9f$ and $1.3f$. These experiments are the ones forced by the relatively strong winds, which are listed in the first row of Table 1. As shown in Fig. 7, the bottom mixing at the offshore side is indeed enhanced in the critical case with $\omega = \omega_{\text{SCR}} = 1.1f$. More interestingly, enhanced mixing is also found in some near-critical cases, specifically the cases with $\omega = 1.05f$ and $1.0f$. However, such mixing enhancement is not obvious in other near-critical cases with $\omega > \omega_{\text{SCR}}$. To better show this asymmetric response, we exhibit the dissipation rate as a function of across-shore distance and wave frequency (Fig. 8a) by utilizing the experiments with refined frequencies near ω_{SCR} (Table 1). The dissipation rate shown in Fig. 8a is averaged over 5 m above the bottom and over 10 days. The result indicates that the strongest mixing occurs at the locations associated with critical/near-critical reflection (i.e., between -100 and -80 km; cf. the ray-tracing solutions in Fig. 6), thus suggests that the critical/near-critical reflection of NIWs leads to the enhancement of mixing. In addition, the

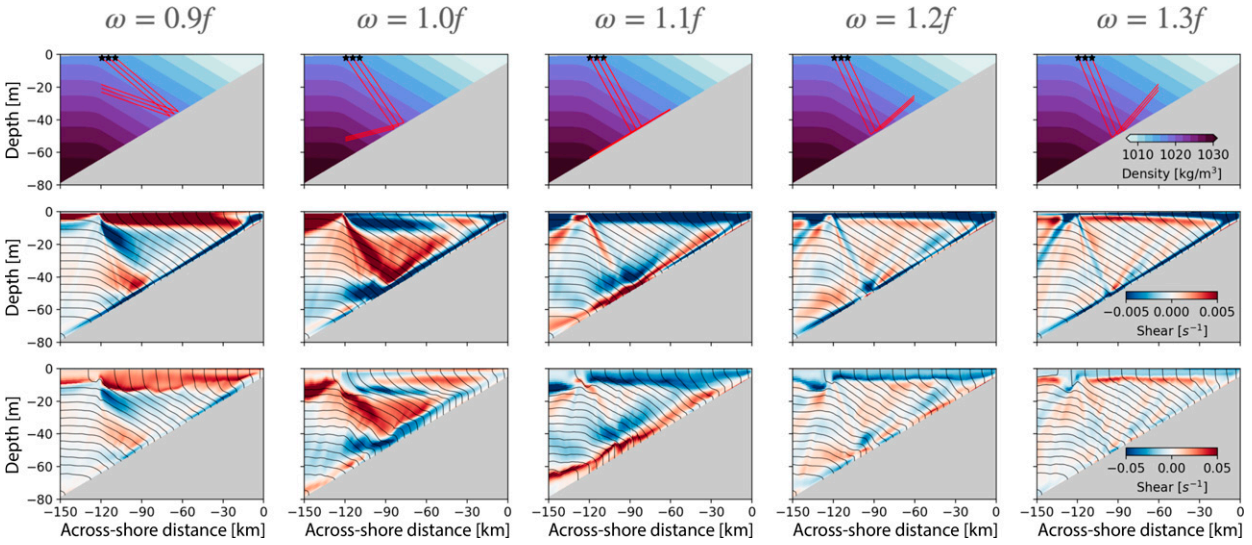

FIG. 6. (top) Rays (red lines) of the NIWs with the frequencies ranging from $0.9f$ to $1.3f$. The initial density field of the idealized model is shaded. (middle) Across-shore sections of $\partial u/\partial z$ from the idealized simulations with the weak wind forcing (4×10^{-3} N m^{-2}); u is the across-shore velocity. (bottom) Across-shore sections of $\partial u/\partial z$ from the idealized simulations with the stronger wind forcing (4×10^{-2} N m^{-2}). These snapshots are made at $t = 240$ h. Isopycnals are contoured in gray every 1.0 kg m^{-3}.

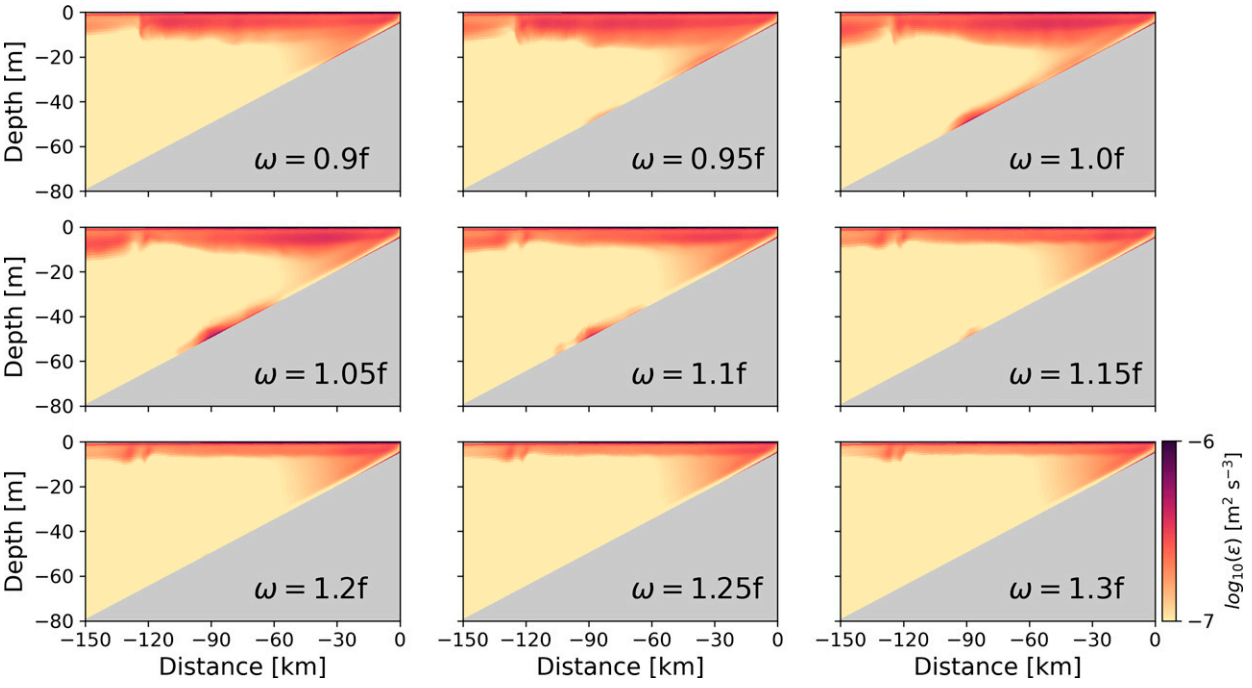

FIG. 7. Across-shore sections of TKE dissipation rate ϵ from the simulations with the wind frequencies ranging from $0.9f$ to $1.3f$; ϵ is averaged over 10 days. The selected simulations are forced by the stronger winds (4×10^{-2} N m^{-2}), and they are a subset of the simulations listed in the first row of Table 1.

enhancement of mixing is not centered at the critical frequency ($1.1f$) but slightly shifts toward lower frequencies.

To understand the shifted response of bottom mixing, we examine the wind work in the experiments to explore the link between the shifted response of mixing and the energy supply. The wind work indicates the energy input into the NIW field in the surface mixed layer by the oscillatory winds and yields an estimate on the wave energy flux toward the bottom (Whitt and Thomas 2015; Qu et al. 2021a). It is defined as

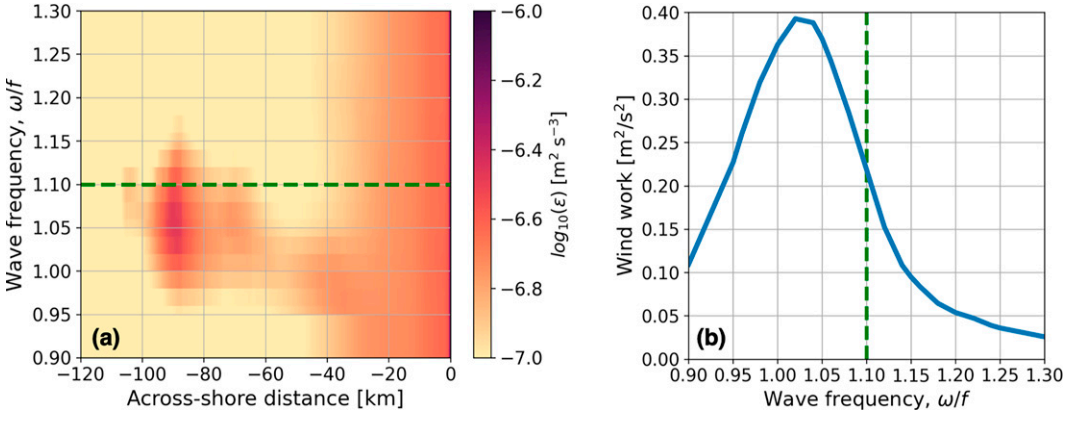

FIG. 8. (a) TKE dissipation rate ϵ as a function of across-shore distance and wave frequency. This is made using the simulations forced by the stronger winds (4×10^{-2} N m^{-2}). In each simulation, ϵ is calculated by averaging it over 5 m above the bottom and over 10 days, yielding one single across-shore profile. Each profile is tagged with the wave frequency of the corresponding simulation and then integrated to get the plot shown. (b) Wind work as a function of wave frequency. The wind work is evaluated in each simulation and tagged with the corresponding wave frequency. The green dashed lines in (a) and (b) denote the critical frequency $\omega_{SCR} = 1.1f$. The wave frequencies associated with the simulations are listed in the first row of Table 1.

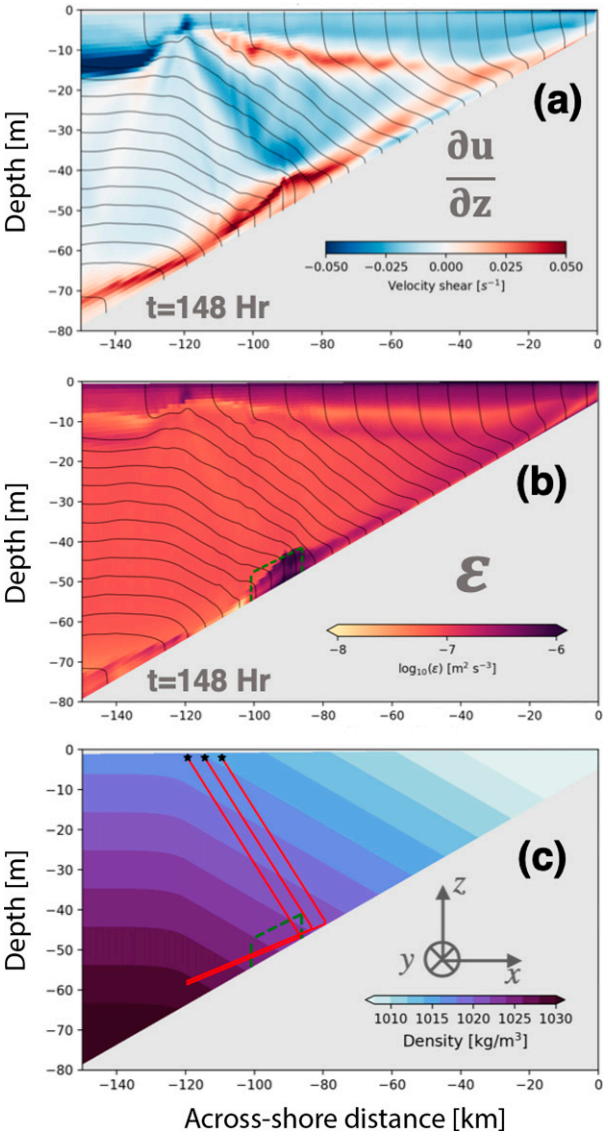

FIG. 9. Across-shore sections of (a) vertical shear $\partial u/\partial z$ and (b) TKE dissipation rate ϵ from the base run. These sections are made at $t = 148$ h. Isopycnals are contoured in gray every 1.0 kg m^{-3}. (c) Rays (red lines) of the NIWs with a frequency of 1.048f (equivalent to a period of 24 h). The black stars denote the initial locations of the waves. The initial density field is shaded. A control volume, where the mixing is enhanced, is outlined by the green dashed lines in (b) and (c) for the analysis in Fig. 10, below.

$$\text{wind work} = \overline{\int_T \frac{\boldsymbol{\tau} \cdot \mathbf{u}_{\mathrm{ML}}}{\rho_0 H_{\mathrm{ML}}}\, dt}, \tag{7}$$

where $\boldsymbol{\tau}$ is the wind stress, $\mathbf{u}_{\mathrm{ML}}$ is the mixed layer velocity, $\rho_0 = 1025$ kg m^{-3} is the reference density, $H_{\mathrm{ML}} = 10$ m is the mixed layer thickness, $T = 10$ days is the integration period, and the overbar represents the lateral average. The wind work is evaluated in each experiment and is shown as a function of wave frequency in Fig. 8b. The curve of the wind work deviates from $\omega_{\mathrm{SCR}} = 1.1f$ with its maximum near the inertial frequency f, presumably due to the resonance with the inertial frequency. In other words, the winds with frequencies closer to f input more energy into the NIW field and facilitate more intense bottom mixing during near-critical reflection of the NIWs, suggestive of a mechanism inducing the shifted response of bottom mixing.

c. *Mechanism driving the near-inertially enhanced mixing*

To explore the mechanism driving the near-inertially enhanced mixing, we mimic the scenario over the Texas–Louisiana shelf by forcing the idealized model by diurnal, land–sea breeze–like winds. The winds are oriented in the across-shore direction and rectilinearly oscillate with a frequency of $\omega = 1.048f$ (equivalent to a period of 24 h) and an amplitude of 4×10^{-2} N m^{-2}. This simulation is hereinafter referred to as the base run. Since ω is close to $\omega_{\mathrm{SCR}} = 1.1f$, the NIWs generated by the winds should undergo near-critical reflection off the bottom.

Consistent with the realistic simulation, the near-inertially enhanced bottom mixing is also found in the base run. Snapshots of the vertical shear and TKE dissipation rate ϵ at $t = 148$ h when the mixing is prominently enhanced are shown in Fig. 9. The pattern of the vertical shear resembles the pathway of the NIWs predicted by the ray-tracing solution, suggestive of active near-critical reflection. The dissipation at the wave-focusing region is significantly elevated being one order of magnitude higher than ambient values. The dissipation averaged over the control volume exhibits near-inertial pulsing, indicating that the bottom mixing is near-inertially enhanced. The underlying mechanism associated with the NIWs and the near-inertially enhanced bottom mixing is discussed below.

Upon the near-critical reflection, the wave energy is focused near the bottom, and the wave amplitudes are amplified, evidenced by the enhanced vertical shear shown in Fig. 9a. However, the bottom mixing is preferentially enhanced at a certain phase of the shear. In comparing Figs. 10a and 10b, we can see that ϵ pulses when the across-shore shear $\partial u/\partial z$ approaches its maxima. Noticing that the across-shore buoyancy gradient is positive over the shelf (i.e., $\partial b/\partial x > 0$), a vertically sheared flow with $\partial u/\partial z > 0$ would advect dense water over light, destratify the fluid, and further facilitate the mixing on top of the wave amplification.

To quantify the impact of the vertical shear on destratification, we evaluate the contribution of the horizontal differential advection of buoyancy $-(\partial u/\partial z)(\partial b/\partial x)$ to the evolution of N^2. The evaluation is conducted at the wave-focusing region (outlined by the dashed green lines in Figs. 9 and 10). As shown in Fig. 10c, the fluid is indeed near-inertially destratified. This near-inertially modulated destratification is represented by a near-inertial variation in $\partial N^2/\partial t$ (Fig. 10d). More important, the variations of $\partial N^2/\partial t$ are dominated by $-(\partial u/\partial z)(\partial b/\partial x)$ (Fig. 10d), suggesting that the across-shore shear is the major factor inducing the destratification via differential advection. The process of such destratification is shown in Figs. 10f and 10g. The near-inertial destratification results in the near-inertial reduction of the Richardson number (Fig. 10e). The combined effect of the near-inertially reduced Richardson number and

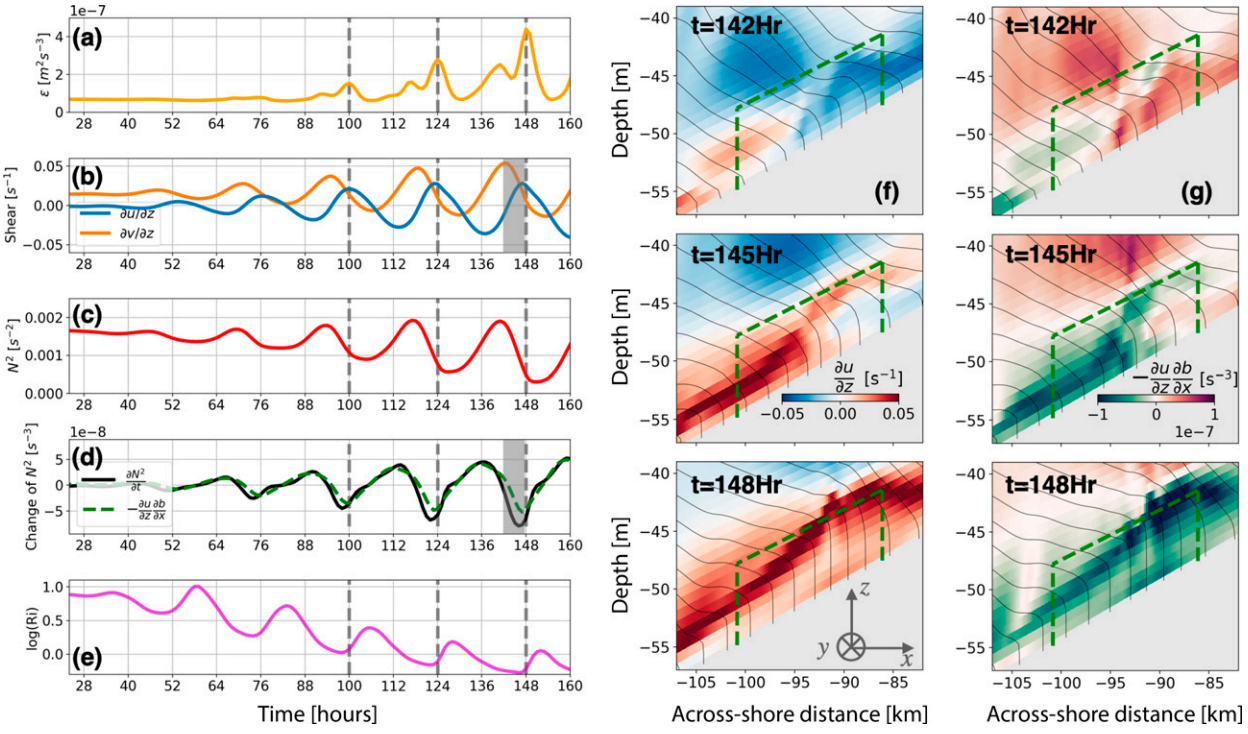

FIG. 10. Time series of TKE (a) dissipation rate, (b) vertical shear, (c) stratification, (d) diagnostic terms of stratification, and (e) Richardson number. All of these quantities are averaged over the control volume outlined in (f) and (g) by the green dashed lines; t = 100, 124, and 148 h are marked by the vertical gray dashed lines, denoting the time with enhanced mixing. Also shown are across-shore sections of (f) $\partial u/\partial z$ and (g) $-(\partial u/\partial z)(\partial b/\partial x)$ during a destratification process. The sections are made in the period from t = 142 to 148 h, which is shaded in (b) and (d). Isopycnals are contoured in gray every 0.5 kg m^{-3}.

the enhanced shear (due to wave focusing) leads to the near-inertially enhanced mixing via the k–ϵ turbulent closure model.

A kinetic energy budget is made at the wave-focusing region to demonstrate the link between the NIWs and the enhanced mixing. The energetics analysis involves the kinetic energy equation as follows:

$$\underbrace{\frac{\partial}{\partial t}\overline{\mathrm{KE}}}_{\mathrm{TRC}} = \underbrace{-\overline{\mathbf{u}\cdot\nabla\mathrm{KE}}}_{\mathrm{ADV}} \underbrace{-\nabla\cdot\left(\overline{\frac{p'}{\rho_0}\mathbf{u}'}\right)}_{\mathrm{WEF}} + \underbrace{\overline{w'b'}}_{\mathrm{WBF}} \underbrace{-\nabla\cdot\left(\frac{\overline{p}}{\rho_0}\overline{\mathbf{u}}\right)}_{\mathrm{MEF}}$$

$$+ \underbrace{\overline{w}\,\overline{b}}_{\mathrm{MBF}} \underbrace{-\overline{\nu(u_z^2+v_z^2)}}_{\mathrm{DKE}} + \underbrace{\overline{\frac{\partial}{\partial z}\left(\nu\frac{\partial \mathrm{KE}}{\partial z}\right)}}_{\mathrm{RKE}},$$

where KE = $0.5(u^2 + v^2)$ is the kinetic energy, the overbars represent a temporal average with a window of 24 h (equivalent to the wave frequency $\omega = 1.048f$), the barred variables are associated with the mean field, and the primed variables are associated with the wave field. The kinetic energy budget is shown in Fig. 11. The WEF term (representing the convergence of wave energy flux) is the dominant energy source, while the DKE (representing the loss of kinetic energy to turbulence) is the dominant energy sink. It implies that the energy sustaining the turbulence and mixing is mainly supplied by the NIWs.

5. Discussion

One important impact of the slantwise critical reflection of NIWs on the environments over the seafloor is enhanced turbulent transport of tracers in bottom boundary layers. Here, we take the Texas–Louisiana shelf as an example to illustrate this impact. The shelf is known to be prone to bottom hypoxia, because the freshwater input from the Mississippi River and Atchafalaya River suppresses ventilation of bottom waters (Hetland and DiMarco 2008; Bianchi et al. 2010). Bottom boundary layer dynamics are critical in the formation and ventilation of the hypoxia over the shelf. Both observations (DiMarco et al. 2010; Zimmerle and DiMarco 2016) and numerical experiments (Zhang and Hetland 2018) show patchiness in bottom oxygen distributions with similar spatial scales as the eddy field over the shelf, 10–50 km. A recent study shows that the temporal evolution of bottom hypoxia exhibits significant near-inertial variability (Ruiz Xomchuk et al. 2021), suggestive of active modulations by NIWs. In this study, we will further demonstrate that the critical reflection of NIWs off the shelf can ventilate the bottom low-oxygen water via enhancing the turbulent flux of oxygen into the bottom boundary layer.

In the realistic model, a benthic layer with low concentration of oxygen is found in the region associated with the critical reflection of NIWs (Fig. 12b). In this region, the diffusivity κ is significantly higher than in the surrounding area due to the NIW enhancement of mixing (Fig. 12a). This leads to an

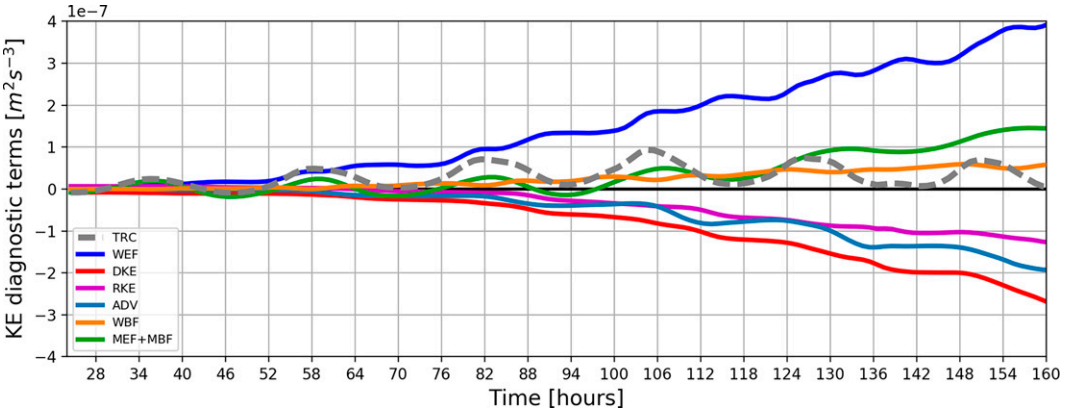

FIG. 11. Kinetic energy budget in the control volume marked in Fig. 10f. TRC is the rate-of-change term. ADV is the advection of kinetic energy. RKE and DKE are the redistribution and dissipation of kinetic energy by turbulence, respectively. The total flux of kinetic energy is decomposed into a wave-related term WEF (representing the convergence of wave energy flux) and a mean flow-related term MEF (representing the mean energy flux convergence). Similarly, the total buoyancy flux is decomposed into the wave buoyancy flux WBF and the mean buoyancy flux MBF. All of the terms are averaged over the control volume.

elevated, downward oxygen flux $\langle w'o' \rangle = -\kappa(\partial o/\partial z)$, where o is the concentration of oxygen (Fig. 12c). Also, the time series of κ and $\langle w'o' \rangle$ show clear signals of intensification at the period when mixing is enhanced, that is, from 6 to 9 June (Figs. 12d,e). The elevated $\langle w'o' \rangle$ represents the oxygenation, with a rate of $O(10)$ mmol m^{-2} day^{-1}, and this rate is comparable to the sediment oxygen consumption rate observed over the shelf, which is around 2 mmol m^{-2} day^{-1} at the oxygen concentration range of 100–200 mmol m^{-3} (Rowe et al. 2002). This indicates that, upon the critical reflection, the turbulence is energized, leading to an enhanced downward transport of oxygen and ventilation of the bottom low-oxygen water.

To complement the realistic simulation, a tracer experiment was run using the idealized flow configuration to demonstrate this ventilation process by NIWs. A bottom-depleted passive tracer is added to the base run. The initial field of the tracer is shown in Fig. 13. The tracer concentration exponentially decreases in the vertical direction and has no gradient across the slope, representing a uniform layer of low tracer concentration over the slope. There are no tracer fluxes at the top and bottom boundaries. The evolution of this bottom layer is monitored during the slantwise critical reflection of NIWs. Also, a comparative run without wind forcing (so without NIWs) is conducted to highlight the ventilation by NIWs.

Here, we only focus on the wave-focusing region close to the bottom, which is shown in Fig. 13a. The diffusivity and turbulent tracer flux are compared between the wind-on and wind-off cases. Figure 14 shows the snapshots of the

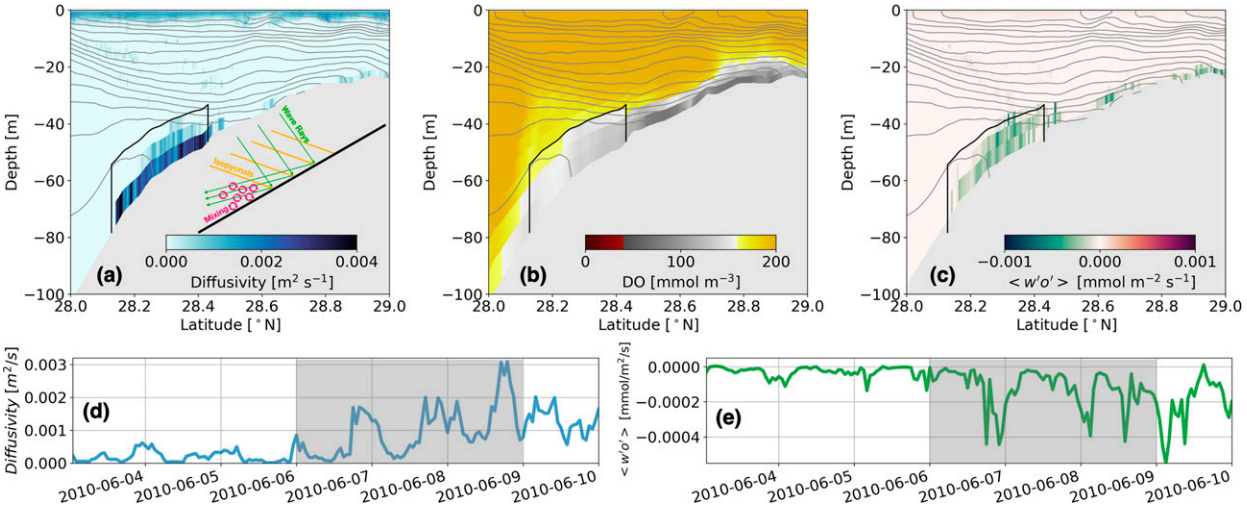

FIG. 12. Across-shore sections of (a) diffusivity, (b) concentration of DO, and (c) turbulent oxygen flux along the section marked in Fig. 1c. These properties are averaged between 6 and 9 Jun, when the bottom mixing is enhanced. The period is shaded in (d) and (e). Isopycnals are contoured in gray every 0.5 kg m^{-3}. The control volume encompassed by the black lines is the same region marked in Fig. 2d, where the mixing is enhanced. Also shown are time series of the (d) diffusivity and (e) turbulent oxygen flux averaged over the control volume.

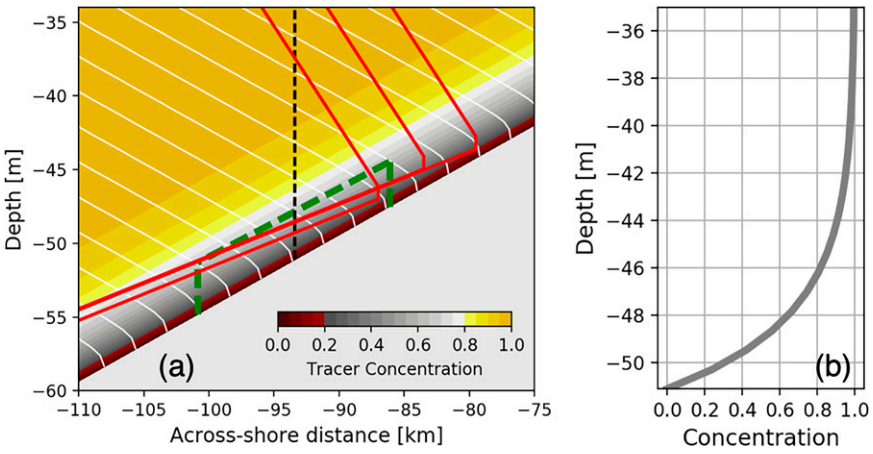

FIG. 13. (a) Initial condition of passive tracer. The red lines are the ray-tracing solutions shown in Fig. 9c. The control volume selected for later analysis is denoted by the green dashed lines. Isopycnals are contoured in white every 0.5 kg m^{-3}. (b) Profile of tracer concentration along the black dashed line marked in (a).

comparison at the time when the bottom mixing is prominently enhanced by the NIWs. The wind-on case shows much higher diffusivity and stronger turbulent tracer fluxes than the wind-off case at the wave-focusing region. This indicates a ventilating influence to the bottom boundary layer induced by the NIWs. Furthermore, the diagnostics of the tracer evolution show that, in the wind-on case, the vertical diffusion term is near-inertially enhanced, and the rate-of-change term is dominated by the

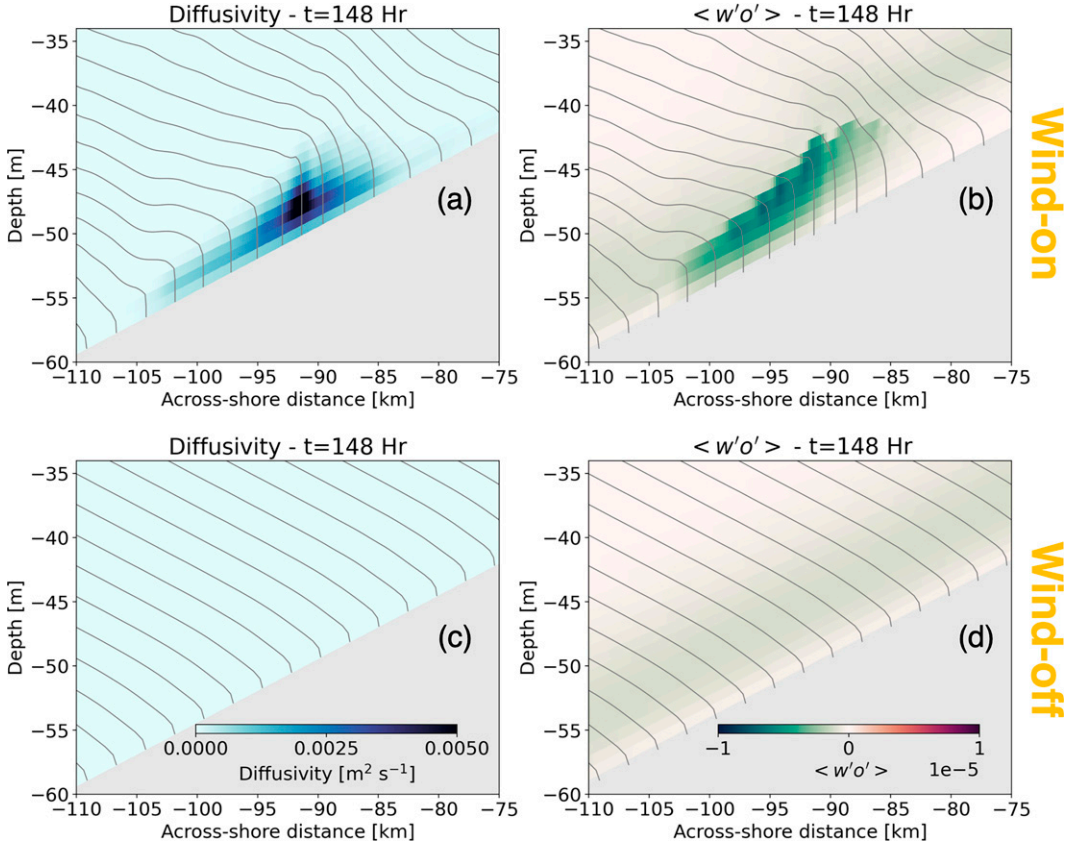

FIG. 14. Across-shore sections of (left) diffusivity and (right) turbulent tracer flux at t = 148 h in the (a),(b) wind-on and (c),(d) wind-off cases. Isopycnals are contoured in gray every 0.5 kg m^{-3}.

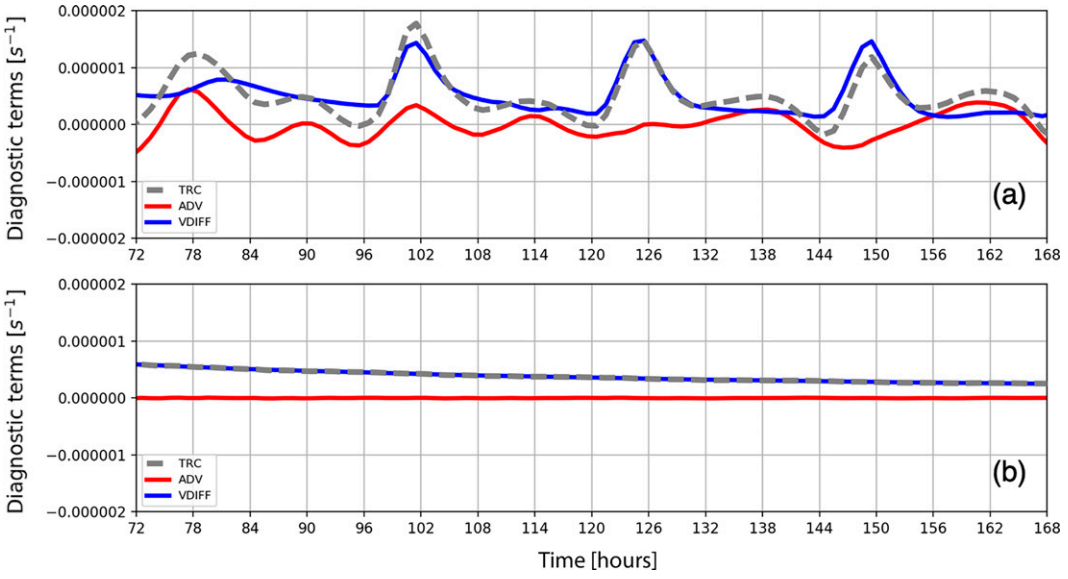

FIG. 15. Diagnostic terms of the tracer equation in the (a) wind-on and (b) wind-off cases. TRC = $\overline{\partial C/\partial t}$ is the rate of change, ADV = $\overline{\mathbf{u} \cdot \nabla C}$ is the advection term, and VDIFF = $\overline{\partial/\partial z[\kappa(\partial C/\partial z)]}$ is the vertical diffusion term, where C is the tracer concentration, and the overbar represents a volume average. These properties are averaged over the control volume outlined in Fig. 13 by the green dashed lines.

vertical diffusion term (Fig. 15a). In contrast, the vertical diffusion (i.e., the background diffusion) in the wind-off case does not exhibit any near-inertial pulsing feature, not surprisingly (Fig. 15b). The timing of the near-inertial enhancement of the vertical diffusion is consistent with the time of the mixing enhancement shown in Fig. 10a. Consequently, it can be inferred that the enhanced ventilation revealed in the wind-on case is caused by the slantwise critical reflection of the NIWs.

6. Conclusions

Using the Texas–Louisiana shelf as an example, the study demonstrates that bottom mixing over a continental shelf can be enhanced via slantwise critical reflection of wind-driven NIWs. This is a specific scenario of inertia gravity wave-driven mixing in the coastal ocean, a relatively understudied type in comparison with its counterpart—the critical reflection of internal tides off sloping bathymetry (Cacchione et al. 2002; Nash et al. 2004; Martini et al. 2011). The NIWs over the Texas–Louisiana shelf are near-resonantly forced by the diurnal land–sea breeze and can efficiently radiate downward at sharp fronts in the river plume. The downward-propagating NIWs are focused near the bottom upon slantwise critical reflection, and the mixing is correspondingly enhanced in the bottom boundary layer. Interestingly, the mixing enhancement exhibits a feature of near-inertial pulsing.

The mechanism driving the near-inertially enhanced mixing is investigated in an idealized simulation. Because of the slantwise critical reflection, the wave energy is focused and amplified near the bottom, leading to enhanced vertical shear. On top of the enhanced shear, the bottom mixing is preferentially enhanced at the phases with the shear destratifying the fluid. In the presence of the horizontal buoyancy gradients, the vertically sheared flow can advect dense water over light. As a consequence, the fluid is periodically destratified. The combined effect of the enhanced shear and the periodic destratification induces the near-inertially enhanced mixing. This mechanism of the periodic destratification is analogous to the internal seiching in a lake (Lorke et al. 2005) and the strain-induced periodic stratification (SIPS) in a tide-influenced estuary, where the tidal variability of stratification and mixing is caused by differential advection in the presence of tidal straining (Simpson et al. 1990; Geyer and MacCready 2014).

In addition to the mechanism of slantwise critical reflection, bottom mixing over a sloping bathymetry can also be enhanced by NIWs via the mechanism of "slantwise critical layers" (Qu et al. 2021b). The fundamental difference between these two mechanisms is the conceptual configuration. A slantwise critical layer is a trapping zone for NIWs where isopycnals run parallel with a sloping bathymetry, whereas a scenario of slantwise critical reflection involves isopycnals intersecting with a sloping bathymetry. The difference of the configuration leads to two distinct mechanisms driving the enhanced mixing. In a slantwise trapping zone, the group velocity of the NIWs decreases to zero, and the waves then become trapped, leading to accumulated wave energy and enhanced mixing. In contrast, in the scenario of slantwise critical reflection, the NIWs are not trapped (i.e., the group velocity is not equal to zero) but amplified, and the enhanced mixing is not only due to the amplified across-slope shear but also the associated destratification (by differential advection), latter of which is absent in a slantwise trapping zone because of the absence of across-slope buoyancy gradients.

The criterion for slantwise critical reflection of NIWs is derived based on a simple theoretical model, which consists of three elements: a bottom-attached front, a shelf, and downward-propagating NIWs. The criterion is

$$\omega_{\mathrm{SCR}} = \sqrt{f^2 + s_{\mathrm{bot}}^2 N^2 (1 - s_\rho / s_{\mathrm{bot}})},$$

revealing that the front, bathymetry, and rotation set the frequency of the NIWs undergoing slantwise critical reflection. If the wave frequency is less than or greater than ω_{SCR}, the NIWs would undergo backward or forward reflection, respectively. The criterion is derived on the basis of an assumption that the mean flow is in the thermal wind balance and only varies in the slope-normal direction. This assumption yields a cleaner criterion than Federiuk and Allen (1996) but may restrict its application under certain scenarios (e.g., a barotropic flow that varies in the cross-shore direction).

Slantwise critical reflection of NIWs has important environmental implications in the coastal ocean since turbulent transport of tracers can be enhanced during the process. On the Texas–Louisiana shelf, the bottom boundary layer can be hypoxic because of lack of ventilation. Both the realistic and idealized simulations indicate that the slantwise critical reflection of NIWs could enhance downward turbulent oxygen flux and therefore act as a ventilating process for the bottom low-oxygen water.

Acknowledgments. This work was funded by the SUNRISE project, NSF Grants OCE-1851450 (to authors Qu and Thomas) and OCE-1851470 (to authors Hetland and Kobashi), and supported by the Earth System Model Development and Regional and Global Modeling and Analysis program areas of the U.S. Department of Energy Office of Science and Office of Biological and Environmental Research as part of the multiprogram, collaborative Integrated Coastal Modeling (ICoM) project. We thank Bertrand Delorme, Jamie Hilditch, and two anonymous reviewers for very helpful suggestions while we were preparing this paper.

Data availability statement. The data of the realistic and idealized simulations are available online (https://doi.org/10.5281/zenodo.6469286). The code used for the ray-tracing calculation is also available online (https://github.com/LixinQu/Ray-Tracing.git).

APPENDIX

The Rotated Coordinate System

The coordinate system is rotated to align with the linear slope. In the rotated coordinates, the across-slope coordinate $\hat{x}$ aligns the slope and is defined positive toward shallower depths, and the slope-normal coordinate $\hat{z}$ is defined positive upward. The relation between the nonrotated and rotated coordinates is

$$\hat{x} = x\cos\theta + z\sin\theta \quad \text{and}$$

$$\hat{z} = -x\sin\theta + z\cos\theta, \tag{A1}$$

where θ is the slope angle.

Based on the configuration of the theoretical model, the background velocity $\overline{v}$ is a function only of the slope-normal coordinate $\hat{z}$ (i.e., $\partial\overline{v}/\partial\hat{x} = 0$). Consequently, the velocity gradients in the nonrotated and rotated coordinates can be linked by the following equations:

$$\frac{\partial\overline{v}}{\partial x} = \frac{\partial\overline{v}}{\partial\hat{z}}\frac{\partial\hat{z}}{\partial x} = -\frac{\partial\overline{v}}{\partial\hat{z}}\sin\theta \quad \text{and}$$

$$\frac{\partial\overline{v}}{\partial z} = \frac{\partial\overline{v}}{\partial\hat{z}}\frac{\partial\hat{z}}{\partial z} = \frac{\partial\overline{v}}{\partial\hat{z}}\cos\theta, \tag{A2}$$

Applying the thermal wind balance $\partial\overline{v}/\partial z = M^2 f^{-1}$ into Eq. (A2), the horizontal gradient of $\overline{v}$ can be expressed as

$$\partial\overline{v}/\partial x = -M^2 f^{-1} s_{\mathrm{bot}}. \tag{A3}$$

It reveals that the background flow is horizontally sheared and that its shear is determined by the bottom slope $s_{\mathrm{bot}} \equiv \tan\theta$, the horizontal buoyancy gradient $M^2 \equiv \partial\overline{b}/\partial x$, and the Coriolis parameter f.

REFERENCES

Asselin, O., and W. R. Young, 2020: Penetration of wind-generated near-inertial waves into a turbulent ocean. *J. Phys. Oceanogr.*, **50**, 1699–1716, https://doi.org/10.1175/JPO-D-19-0319.1.

Bianchi, T. S., S. F. DiMarco, J. H. Cowan Jr., R. D. Hetland, P. Chapman, J. W. Day, and M. A. Allison, 2010: The science of hypoxia in the northern Gulf of Mexico: A review. *Sci. Total Environ.*, **408**, 1471–1484, https://doi.org/10.1016/j.scitotenv.2009.11.047.

Brink, K. H., 1991: Coastal-trapped waves and wind-driven currents over the continental shelf. *Annu. Rev. Fluid Mech.*, **23**, 389–412, https://doi.org/10.1146/annurev.fl.23.010191.002133.

Cacchione, D., L. F. Pratson, and A. S. Ogston, 2002: The shaping of continental slopes by internal tides. *Science*, **296**, 724–727, https://doi.org/10.1126/science.1069803.

Canuto, V. M., A. Howard, Y. Cheng, and M. Dubovikov, 2001: Ocean turbulence. Part I: One-point closure model—Momentum and heat vertical diffusivities. *J. Phys. Oceanogr.*, **31**, 1413–1426, https://doi.org/10.1175/1520-0485(2001)031<1413:OTPIOP>2.0.CO;2.

Chant, R. J., 2001: Evolution of near-inertial waves during an upwelling event on the New Jersey inner shelf. *J. Phys. Oceanogr.*, **31**, 746–764, https://doi.org/10.1175/1520-0485(2001)031<0746:EONIWD>2.0.CO;2.

Chapman, D. C., and S. J. Lentz, 1994: Trapping of a coastal density front by the bottom boundary layer. *J. Phys. Oceanogr.*, **24**, 1464–1479, https://doi.org/10.1175/1520-0485(1994)024<1464:TOACDF>2.0.CO;2.

Dee, D. P., and Coauthors, 2011: The ERA-Interim reanalysis: Configuration and performance of the data assimilation system. *Quart. J. Roy. Meteor. Soc.*, **137**, 553–597, https://doi.org/10.1002/qj.828.

DiMarco, S. F., and R. O. Reid, 1998: Characterization of the principal tidal current constituents on the Texas-Louisiana shelf. *J. Geophys. Res.*, **103**, 3093–3109, https://doi.org/10.1029/97JC03289.

——, M. K. Howard, and R. O. Reid, 2000: Seasonal variation of wind-driven diurnal current cycling on the Texas-Louisiana

continental shelf. *Geophys. Res. Lett.*, **27**, 1017–1020, https://doi.org/10.1029/1999GL010491.

——, P. Chapman, N. Walker, and R. D. Hetland, 2010: Does local topography control hypoxia on the eastern Texas–Louisiana shelf? *J. Mar. Syst.*, **80**, 25–35, https://doi.org/10.1016/j.jmarsys.2009.08.005.

Federiuk, J., and J. S. Allen, 1996: Model studies of near-inertial waves in flow over the Oregon continental shelf. *J. Phys. Oceanogr.*, **26**, 2053–2075, https://doi.org/10.1175/1520-0485(1996)026<2053:MSONIW>2.0.CO;2.

Fennel, K., and Coauthors, 2016: Effects of model physics on hypoxia simulations for the northern Gulf of Mexico: A model intercomparison. *J. Geophys. Res. Oceans*, **121**, 5731–5750, https://doi.org/10.1002/2015JC011577.

Geyer, W. R., and P. MacCready, 2014: The estuarine circulation. *Annu. Rev. Fluid Mech.*, **46**, 175–197, https://doi.org/10.1146/annurev-fluid-010313-141302.

Grisouard, N., and L. N. Thomas, 2015: Critical and near-critical reflections of near-inertial waves off the sea surface at ocean fronts. *J. Fluid Mech.*, **765**, 273–302, https://doi.org/10.1017/jfm.2014.725.

Hetland, R. D., 2005: Relating river plume structure to vertical mixing. *J. Phys. Oceanogr.*, **35**, 1667–1688, https://doi.org/10.1175/JPO2774.1.

——, 2017: Suppression of baroclinic instabilities in buoyancy-driven flow over sloping bathymetry. *J. Phys. Oceanogr.*, **47**, 49–68, https://doi.org/10.1175/JPO-D-15-0240.1.

——, and S. F. DiMarco, 2008: How does the character of oxygen demand control the structure of hypoxia on the Texas–Louisiana continental shelf? *J. Mar. Syst.*, **70**, 49–62, https://doi.org/10.1016/j.jmarsys.2007.03.002.

——, and ——, 2012: Skill assessment of a hydrodynamic model of circulation over the Texas–Louisiana continental shelf. *Ocean Modell.*, **43–44**, 64–76, https://doi.org/10.1016/j.ocemod.2011.11.009.

Jacox, M. J., and C. A. Edwards, 2011: Effects of stratification and shelf slope on nutrient supply in coastal upwelling regions. *J. Geophys. Res.*, **116**, C03019, https://doi.org/10.1029/2010JC006547.

Kobashi, D., and R. Hetland, 2020: Reproducibility and variability of submesoscale frontal eddies on a broad, low-energy shelf of freshwater influence. *Ocean Dyn.*, **70**, 1377–1395, https://doi.org/10.1007/s10236-020-01401-4.

Kunze, E., 1985: Near-inertial wave propagation in geostrophic shear. *J. Phys. Oceanogr.*, **15**, 544–565, https://doi.org/10.1175/1520-0485(1985)015<0544:NIWPIG>2.0.CO;2.

——, and S. G. L. Smith, 2004: The role of small-scale topography in turbulent mixing of the global ocean. *Oceanography*, **17**, 55–64, https://doi.org/10.5670/oceanog.2004.67.

Lee, D.-K., and P. P. Niiler, 1998: The inertial chimney: The near-inertial energy drainage from the ocean surface to the deep layer. *J. Geophys. Res.*, **103**, 7579–7591, https://doi.org/10.1029/97JC03200.

Lerczak, J. A., M. Hendershott, and C. D. Winant, 2001: Observations and modeling of coastal internal waves driven by a diurnal sea breeze. *J. Geophys. Res.*, **106**, 19 715–19 729, https://doi.org/10.1029/2001JC000811.

Lorke, A., F. Peeters, and A. Wüest, 2005: Shear-induced convective mixing in bottom boundary layers on slopes. *Limnol. Oceanogr.*, **50**, 1612–1619, https://doi.org/10.4319/lo.2005.50.5.1612.

MacCready, P., and P. B. Rhines, 1991: Buoyant inhibition of Ekman transport on a slope and its effect on stratified spin-up. *J. Fluid Mech.*, **223**, 631–661, https://doi.org/10.1017/S0022112091001581.

MacKinnon, J. A., and M. C. Gregg, 2005: Near-inertial waves on the New England shelf: The role of evolving stratification, turbulent dissipation, and bottom drag. *J. Phys. Oceanogr.*, **35**, 2408–2424, https://doi.org/10.1175/JPO2822.1.

——, and Coauthors, 2017: Climate Process Team on internal wave–driven ocean mixing. *Bull. Amer. Meteor. Soc.*, **98**, 2429–2454, https://doi.org/10.1175/BAMS-D-16-0030.1.

Martini, K. I., M. H. Alford, E. Kunze, S. M. Kelly, and J. D. Nash, 2011: Observations of internal tides on the Oregon continental slope. *J. Phys. Oceanogr.*, **41**, 1772–1794, https://doi.org/10.1175/2011JPO4581.1.

Mooers, C. N. K., 1975: Several effects of a baroclinic current on the cross-stream propagation of inertial-internal waves. *Geophys. Astrophys. Fluid Dyn.*, **6**, 245–275, https://doi.org/10.1080/03091927509365797.

Nash, J. D., E. Kunze, J. M. Toole, and R. W. Schmitt, 2004: Internal tide reflection and turbulent mixing on the continental slope. *J. Phys. Oceanogr.*, **34**, 1117–1134, https://doi.org/10.1175/1520-0485(2004)034<1117:ITRATM>2.0.CO;2.

Qu, L., and R. Hetland, 2020: Nongeostrophic baroclinic instability over sloping bathymetry: Buoyant flow regime. *J. Phys. Oceanogr.*, **50**, 1937–1956, https://doi.org/10.1175/JPO-D-19-0145.1.

——, L. N. Thomas, and J. Gula, 2021a: Bottom mixing enhanced by tropical storm-generated near-inertial waves entering critical layers in the Straits of Florida. *Geophys. Res. Lett.*, **48**, e2021GL093773, https://doi.org/10.1029/2021GL093773.

——, ——, and R. D. Hetland, 2021b: Near-inertial-wave critical layers over sloping bathymetry. *J. Phys. Oceanogr.*, **51**, 1737–1756, https://doi.org/10.1175/JPO-D-20-0221.1.

Ralston, D. K., W. R. Geyer, J. A. Lerczak, and M. Scully, 2010: Turbulent mixing in a strongly forced salt wedge estuary. *J. Geophys. Res.*, **115**, C12024, https://doi.org/10.1029/2009JC006061.

Rowe, G. T., M. E. C. Kaegi, J. W. Morse, G. S. Boland, and E. G. Escobar Briones, 2002: Sediment community metabolism associated with continental shelf hypoxia, northern Gulf of Mexico. *Estuaries*, **25**, 1097–1106, https://doi.org/10.1007/BF02692207.

Ruiz Xomchuk, V., R. D. Hetland, and L. Qu, 2021: Small-scale variability of bottom oxygen in the northern Gulf of Mexico. *J. Geophys. Res. Oceans*, **126**, e2020JC016279, https://doi.org/10.1029/2020JC016279.

Schlosser, T. L., N. L. Jones, C. E. Bluteau, M. H. Alford, G. N. Ivey, and A. J. Lucas, 2019: Generation and propagation of near-inertial waves in a baroclinic current on the Tasmanian shelf. *J. Phys. Oceanogr.*, **49**, 2653–2667, https://doi.org/10.1175/JPO-D-18-0208.1.

Shchepetkin, A. F., and J. C. McWilliams, 2005: The Regional Oceanic Modeling System (ROMS): A split-explicit, free-surface, topography-following-coordinate oceanic model. *Ocean Modell.*, **9**, 347–404, https://doi.org/10.1016/j.ocemod.2004.08.002.

Simpson, J. H., J. Brown, J. Matthews, and G. Allen, 1990: Tidal straining, density currents, and stirring in the control of estuarine stratification. *Estuaries*, **13**, 125–132, https://doi.org/10.2307/1351581.

Smolarkiewicz, P. K., 2006: Multidimensional positive definite advection transport algorithm: An overview. *Int. J. Numer. Methods Fluids*, **50**, 1123–1144, https://doi.org/10.1002/fld.1071.

Stefan, H. G., and E. B. Preud'homme, 1993: Stream temperature estimation from air temperature. *J. Amer. Water Resour. Assoc.*, **29**, 27–45, https://doi.org/10.1111/j.1752-1688.1993.tb01502.x.

Thomas, L. N., J. R. Taylor, R. Ferrari, and T. M. Joyce, 2013: Symmetric instability in the Gulf Stream. *Deep-Sea Res. II*, **91**, 96–110, https://doi.org/10.1016/j.dsr2.2013.02.025.

——, L. Rainville, O. Asselin, W. R. Young, J. Girton, C. B. Whalen, L. Centurioni, and V. Hormann, 2020: Direct observations of near-inertial wave ζ-refraction in a dipole vortex. *Geophys. Res. Lett.*, **47**, e2020GL090375, https://doi.org/10.1029/2020GL090375.

Umlauf, L., and H. Burchard, 2003: A generic length-scale equation for geophysical turbulence models. *J. Mar. Res.*, **61**, 235–265, https://doi.org/10.1357/002224003322005087.

van Meurs, P., 1998: Interactions between near-inertial mixed layer currents and the mesoscale: The importance of spatial variabilities in the vorticity field. *J. Phys. Oceanogr.*, **28**, 1363–1388, https://doi.org/10.1175/1520-0485(1998)028<1363:IBNIML>2.0.CO;2.

Warner, J. C., W. R. Geyer, and J. A. Lerczak, 2005a: Numerical modeling of an estuary: A comprehensive skill assessment. *J. Geophys. Res.*, **110**, C05001, https://doi.org/10.1029/2004JC002691.

——, C. R. Sherwood, H. G. Arango, and R. P. Signell, 2005b: Performance of four turbulence closure models implemented using a generic length scale method. *Ocean Modell.*, **8**, 81–113, https://doi.org/10.1016/j.ocemod.2003.12.003.

Weiss, R. F., 1970: The solubility of nitrogen, oxygen and argon in water and seawater. *Deep-Sea Res. Oceanogr. Abstr.*, **17**, 721–735, https://doi.org/10.1016/0011-7471(70)90037-9.

Whitt, D. B., and L. N. Thomas, 2013: Near-inertial waves in strongly baroclinic currents. *J. Phys. Oceanogr.*, **43**, 706–725, https://doi.org/10.1175/JPO-D-12-0132.1.

——, and ——, 2015: Resonant generation and energetics of wind-forced near-inertial motions in a geostrophic flow. *J. Phys. Oceanogr.*, **45**, 181–208, https://doi.org/10.1175/JPO-D-14-0168.1.

Wijesekera, H. W., J. S. Allen, and P. A. Newberger, 2003: Modeling study of turbulent mixing over the continental shelf: Comparison of turbulent closure schemes. *J. Geophys. Res.*, **108**, 3103, https://doi.org/10.1029/2001JC001234.

Wunsch, C., and R. Ferrari, 2004: Vertical mixing, energy, and the general circulation of the oceans. *Annu. Rev. Fluid Mech.*, **36**, 281–314, https://doi.org/10.1146/annurev.fluid.36.050802.122121.

Xu, K., C. K. Harris, R. D. Hetland, and J. M. Kaihatu, 2011: Dispersal of Mississippi and Atchafalaya sediment on the Texas–Louisiana shelf: Model estimates for the year 1993. *Cont. Shelf Res.*, **31**, 1558–1575, https://doi.org/10.1016/j.csr.2011.05.008.

Yankovsky, A. E., and D. C. Chapman, 1997: A simple theory for the fate of buoyant coastal discharges. *J. Phys. Oceanogr.*, **27**, 1386–1401, https://doi.org/10.1175/1520-0485(1997)027<1386:ASTFTF>2.0.CO;2.

Yankovsky, E., and S. Legg, 2019: Symmetric and baroclinic instability in dense shelf overflows. *J. Phys. Oceanogr.*, **49**, 39–61, https://doi.org/10.1175/JPO-D-18-0072.1.

Young, W., and M. B. Jelloul, 1997: Propagation of near-inertial oscillations through a geostrophic flow. *J. Mar. Res.*, **55**, 735–766, https://doi.org/10.1357/0022240973224283.

Zhang, W., and R. D. Hetland, 2018: A study of baroclinic instability induced convergence near the bottom using water age simulations. *J. Geophys. Res. Oceans*, **123**, 1962–1977, https://doi.org/10.1002/2017JC013561.

Zhang, W. G., T. F. Duda, and I. A. Udovydchenkov, 2014: Modeling and analysis of internal-tide generation and beam-like onshore propagation in the vicinity of shelfbreak canyons. *J. Phys. Oceanogr.*, **44**, 834–849, https://doi.org/10.1175/JPO-D-13-0179.1.

Zhang, X., R. D. Hetland, M. Marta-Almeida, and S. F. DiMarco, 2012: A numerical investigation of the Mississippi and Atchafalaya freshwater transport, filling and flushing times on the Texas-Louisiana Shelf. *J. Geophys. Res.*, **117**, C11009, https://doi.org/10.1029/2012JC008108.

Zhang, Y., A. M. Baptista, and E. P. Myers III, 2004: A cross-scale model for 3D baroclinic circulation in estuary–plume–shelf systems: I. Formulation and skill assessment. *Cont. Shelf Res.*, **24**, 2187–2214, https://doi.org/10.1016/j.csr.2004.07.021.

Zhang, Z., R. Hetland, and X. Zhang, 2014: Wind-modulated buoyancy circulation over the Texas-Louisiana shelf. *J. Geophys. Res. Oceans*, **119**, 5705–5723, https://doi.org/10.1002/2013JC009763.

Zimmerle, H., and S. F. DiMarco, 2016: Mechanisms controlling hypoxia data atlas: High-resolution hydrographic and chemical observations from 2003-2014. *2016 Ocean Sciences Meeting*, New Orleans, LA, Amer. Geophys. Union, Abstract AH44A-0081, https://agu.confex.com/agu/os16/preliminaryview.cgi/Paper90058.html.